

Modeling ULF waves in a compressed dipole magnetic field

A. W. Degeling,¹ R. Rankin,¹ K. Kabin,¹ I. J. Rae,¹ and F. R. Fenrich¹

Received 2 March 2010; revised 20 May 2010; accepted 23 June 2010; published 8 October 2010.

[1] This paper presents the results of a linear model for global scale magneto-hydrodynamic (MHD) waves in a compressed dipole model magnetosphere. We examine scenarios where a localized monochromatic source along the magnetopause boundary launches MHD fast mode ultralow frequency (ULF) waves into the magnetosphere, where they couple to shear Alfvén waves. Sharply peaked field line resonance (FLR) structures are found to form at discrete locations within the magnetosphere in response to the fast mode driver. The extent in local time and relative amplitudes of FLR structures are found to depend strongly on the source location along the magnetopause boundary, indicating how the addition of day/night asymmetry affects the penetration of MHD fast waves within the magnetosphere. This also suggests that observed FLR structures within the magnetosphere may be used to deconvolve the spatial characteristics of the ULF wave source at the magnetopause, giving insight to the excitation mechanism responsible for observed ULF waves. As an example, we consider narrow band ULF activity observed on 25 November 2001 during a high solar wind speed interval following a geomagnetic storm and qualitatively reproduce the spatial and temporal characteristics of observations made by the Prince George SuperDARN radar by constraining the ULF wave source characteristics.

Citation: Degeling, A. W., R. Rankin, K. Kabin, I. J. Rae, and F. R. Fenrich (2010), Modeling ULF waves in a compressed dipole magnetic field, *J. Geophys. Res.*, *115*, A10212, doi:10.1029/2010JA015410.

1. Introduction

[2] It is well known that standing shear Alfvén waves (SAWs) along closed magnetic field lines within the magnetosphere are responsible for many ground-based observations of Pc5 ultralow frequency (ULF) geomagnetic pulsations. Pc5 waves are considered to be an important energy transport mechanism within the magnetosphere, and are thought to play a significant role in radiation belt electron dynamics following geomagnetic storms [e.g., *Elkington*, 2006], auroral arc formation [e.g., *Samson et al.*, 1996; *Rae et al.*, 2007a] and explosive plasma instability during the expansion phase of geomagnetic substorms [e.g., *Dobias et al.*, 2004].

[3] In order to model the relative importance of Pc5 ULF waves in driving, or contributing power to, magnetospheric dynamics, it is important that the properties of the medium through which the waves propagate be adequately represented in the model. Following the groundbreaking analysis of ground-based observations of *Samson et al.* [1971] and initial theoretical work of *Southwood* [1974] and *Chen and Hasegawa* [1974], the propagation properties and generation mechanisms of ULF waves have been investigated extensively, resulting in ULF wave models of

increasing complexity (comprehensive reviews include *Southwood and Hughes* [1983], *Allan and Poulter* [1992], and *Alperovich and Fedorov* [2007]). However most of this work is restricted to dipolar magnetic geometry, or considers SAWs in the absence of coupling across the magnetic field.

[4] This paper presents the results of a model describing the resonant response of magnetic field lines to an externally launched MHD fast wave ULF driver, using a background magnetic field model that includes day/night asymmetry. This extends the work of *Singer et al.* [1981] and *Rankin et al.* [2006] by relaxing the guided Alfvén mode approximation, enabling coupling across magnetic field lines via MHD fast waves. It also generalizes the work of *Allan and Knox* [1979b], *Walker* [1980] and *Degeling and Rankin* [2008] to more realistic magnetic geometry by the inclusion of day/night asymmetry.

[5] The inclusion of day/night asymmetry in the magnetic field model has a number of important effects on ULF wave structure. Firstly, as reported by *Kabin et al.* [2007], the polarization of shear Alfvén wave eigenmodes on closed magnetic field lines becomes dependent on magnetic local time (MLT). Secondly, as we demonstrate in this paper, the accessibility of ULF wave power at a given frequency to different locations within the magnetosphere becomes a function of the source MLT, which affects the coupling of power to field line resonances (FLRs). Both of these issues are of great importance for the energization and transport of radiation belt electrons via the drift resonance mechanism [*Elkington*, 2006]: fast wave accessibility determines the ULF wave power available to interact with the electrons,

¹Department of Physics, University of Alberta, Edmonton, Alberta, Canada.

while the wave polarization affects how the power couples to the electrons.

[6] The rest of this paper is organized as follows: section 2 describes the formulation of the ULF wave equations in a coordinate system aligned with the magnetic field, and shows how these equations may be simplified under the restriction that the background magnetic field has no field-aligned current. An example magnetic field model with this property is introduced, and the method by which the wave equations are solved numerically is summarized, with further details given in Appendix A. Section 3 presents results generated from the model, in which we consider scenarios where ULF waves are excited within the magnetosphere by a ULF wave power source located at the magnetopause. First we demonstrate the effect of varying the location in MLT of the ULF wave source on the relative amplitude of field line resonances excited within the magnetosphere. We then apply the model against observations made during an interval of ULF wave activity on 25 November 2001. Using ground-based observations from the Prince George SuperDARN radar to constrain the spatial characteristics of the ULF wave source for this event, we find source parameters consistent with the hypothesis that the observed FLRs may be driven by Kelvin Helmholtz instability along the afternoon sector magnetopause. Finally, we investigate the equatorial electric field polarization of the FLR excited during this event, and compare against the generalized SAW eigenfunctions of *Rankin et al.* [2006]. Section 4 presents our conclusions.

2. ULF Wave Model

2.1. Cold Plasma MHD Waves

[7] We follow the covariant-contravariant formalism described by *Rankin et al.* [2006] and define a curvilinear coordinate system (α, β, γ) , where α and β are constant on magnetic field lines, such that the magnetic field $\mathbf{B} = B_o \nabla \alpha \times \nabla \beta$ (where B_o is a constant, equal to -3.11×10^{-4} T) and γ is a field-aligned coordinate. In the following we will use the gradient basis vectors $\mathbf{e}^\alpha = \nabla \alpha$, $\mathbf{e}^\beta = \nabla \beta$, $\mathbf{e}^\gamma = \nabla \gamma$, to describe vectors in terms of covariant components (e.g., $\mathbf{E} = E_i \mathbf{e}^i$, where the repeated index implies summation, and i cycles through α, β and γ). The elements of the metric tensor for this basis are given by $g^{ij} = \mathbf{e}^i \cdot \mathbf{e}^j$. Further definitions and explanations of the covariant-contravariant vector components and the metric coefficients are found by *D'haeseleer et al.* [1991] and *Rankin et al.* [2006].

[8] For a cold plasma, assuming ideal magneto-hydrodynamic (MHD) conditions, the wave equations for linear, low-frequency waves are

$$\frac{\partial \mathbf{b}}{\partial t} = -\nabla \times \mathbf{E} \quad (1)$$

$$\frac{1}{v_A^2} \frac{\partial \mathbf{E}}{\partial t} = (\nabla \times \mathbf{b})_\perp - \frac{(\mu_o \mathbf{J} \times \mathbf{b}) \times \mathbf{B}}{B^2}, \quad (2)$$

where \mathbf{b} and \mathbf{E} are perturbed magnetic and electric fields respectively, $\mu_o \mathbf{J} = \nabla \times \mathbf{B}$ is the background current density, and v_A is the Alfvén speed. Following [*Rankin et al.*, 2006],

and noting that $E_\gamma = 0$ for ideal MHD, these equations can be written in component form using the cross product and curl definitions found by *D'haeseleer et al.* [1991]. Equation (1) becomes:

$$g^{\alpha\alpha} \frac{\partial b_\alpha}{\partial t} + g^{\alpha\beta} \frac{\partial b_\beta}{\partial t} + g^{\alpha\gamma} \frac{\partial b_\gamma}{\partial t} = \frac{1}{\sqrt{g}} \frac{\partial E_\beta}{\partial \gamma} \quad (3)$$

$$g^{\beta\alpha} \frac{\partial b_\alpha}{\partial t} + g^{\beta\beta} \frac{\partial b_\beta}{\partial t} + g^{\beta\gamma} \frac{\partial b_\gamma}{\partial t} = -\frac{1}{\sqrt{g}} \frac{\partial E_\alpha}{\partial \gamma} \quad (4)$$

$$g^{\gamma\alpha} \frac{\partial b_\alpha}{\partial t} + g^{\gamma\beta} \frac{\partial b_\beta}{\partial t} + g^{\gamma\gamma} \frac{\partial b_\gamma}{\partial t} = -\frac{1}{\sqrt{g}} \left(\frac{\partial E_\beta}{\partial \alpha} - \frac{\partial E_\alpha}{\partial \beta} \right), \quad (5)$$

while equation (2) becomes:

$$\frac{\sqrt{g}}{v_A^2} \left(g^{\alpha\alpha} \frac{\partial E_\alpha}{\partial t} + g^{\alpha\beta} \frac{\partial E_\beta}{\partial t} \right) = \frac{\partial b_\gamma}{\partial \beta} - \frac{\partial b_\beta}{\partial \gamma} - \sqrt{g} Z^\alpha \quad (6)$$

$$\frac{\sqrt{g}}{v_A^2} \left(g^{\beta\alpha} \frac{\partial E_\alpha}{\partial t} + g^{\beta\beta} \frac{\partial E_\beta}{\partial t} \right) = \frac{\partial b_\alpha}{\partial \gamma} - \frac{\partial b_\gamma}{\partial \alpha} - \sqrt{g} Z^\beta, \quad (7)$$

where Z^α and Z^β are contravariant components of $\mathbf{Z} = (\mu_o \mathbf{J} \times \mathbf{b}) \times \mathbf{B}/B^2$, and g is the determinant of $g_{ij} = [g^{ij}]^{-1}$. Note that $Z^\gamma = g^{ij} Z_j$ and $Z_\gamma = 0$ (by definition).

[9] It can be shown that $E_\gamma = 0$ implies that the third component of equation (2) (for $\partial E^\gamma / \partial t$) contains no additional information and can be derived from the other two components.

[10] We restrict the magnetic field geometry to cases for which $\mathbf{B} \cdot \mathbf{J} = 0$. This allows the magnetic field to be written as

$$\mathbf{B} = B_o \sigma \nabla \gamma, \quad (8)$$

where σ is a scalar function of space [*Ray*, 1963]. In this case it follows immediately that, $B_\alpha = B_\beta = 0$ and $B_\gamma = B_o \sigma$, and it can be shown that $\sqrt{g} = (\sigma g^{\gamma\gamma})^{-1}$. Equation (8) provides a reasonable approximation of Earth's magnetosphere, for example, it occurs naturally if the current density is carried entirely by plasma obeying the guiding center drift equations [*Stern*, 1976]. Under this restriction, it is clear from the definition of \mathbf{B} in terms of Euler potentials α and β that

$$g^{\alpha\gamma} = \nabla \alpha \cdot \nabla \gamma = 0; \quad g^{\beta\gamma} = \nabla \beta \cdot \nabla \gamma = 0. \quad (9)$$

These conditions simplify the wave formalism that will be described in more detail below. With $\mathbf{B} \cdot \mathbf{J} = 0$, the expression for \mathbf{Z} becomes $\mathbf{Z} = \mu_o ((\mathbf{B} \cdot \mathbf{J}) \mathbf{b} - (\mathbf{B} \cdot \mathbf{b}) \mathbf{J}) / B^2 = \mu_o (b_\gamma / (B_o \sigma)) \mathbf{J}$. The contravariant components of \mathbf{J} are given by taking the curl of equation (8), which results in the following expressions for the components of \mathbf{Z}

$$\sqrt{g} Z^\alpha = -\frac{1}{\sigma} \frac{\partial \sigma}{\partial \beta} b_\gamma; \quad \sqrt{g} Z^\beta = \frac{1}{\sigma} \frac{\partial \sigma}{\partial \alpha} b_\gamma. \quad (10)$$

Hence, Z^α and Z^β are both proportional to b_γ .

[11] By taking partial derivatives with respect to γ in equations (3) and (4), and with respect to t in equations (6)

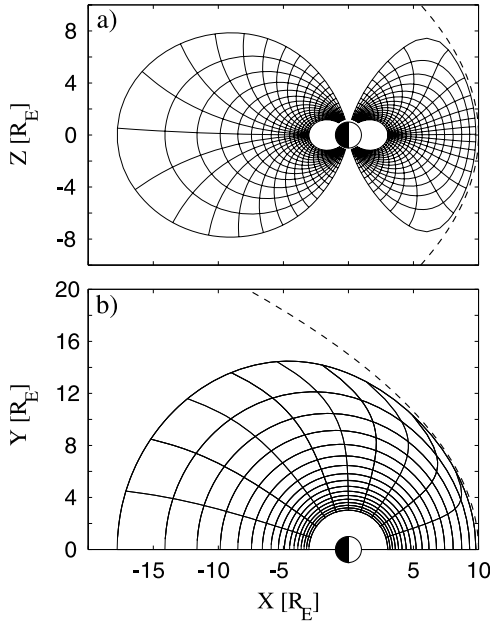


Figure 1. Surfaces of constant α , β , and γ forming the numerical grid for this model, showing (a) the noon meridian and (b) equatorial plane. The dayside magnetopause is indicated by the dashed line.

and (7), then applying equations (9) and (10) to the result, b_α and b_β may be eliminated to give the following:

$$\left(\frac{1}{\sigma}G \cdot \begin{pmatrix} E'_\alpha \\ E'_\beta \end{pmatrix}\right)' - \frac{\sqrt{g}}{v_A^2}G \cdot \begin{pmatrix} \ddot{E}_\alpha \\ \ddot{E}_\beta \end{pmatrix} = \frac{1}{\sigma} \begin{pmatrix} -\partial/\partial\beta(b_\gamma\sigma) \\ \partial/\partial\alpha(b_\gamma\sigma) \end{pmatrix}, \quad (11)$$

where dashes and dots represent partial differentiation with respect to γ and t respectively, and \mathbf{G} is the reduced metric tensor:

$$G = \begin{pmatrix} g^{\alpha\alpha} & g^{\alpha\beta} \\ g^{\alpha\beta} & g^{\beta\beta} \end{pmatrix}. \quad (12)$$

Applying equation (9) to equation (5) then gives b_γ in terms of the components of \mathbf{E} :

$$\dot{b}_\gamma = -\sigma \left(\frac{\partial E_\beta}{\partial \alpha} - \frac{\partial E_\alpha}{\partial \beta} \right). \quad (13)$$

Note that the left hand side of equation (11) contains only field aligned spatial (and time) derivatives of the components of \mathbf{E} , whereas the right hand side is a function of b_γ only. If b_γ is ignorable, the coupling across field lines is removed and, assuming the electric field varies as $\exp(-i\omega t)$, the resulting second-order homogeneous equation gives the shear Alfvén wave eigenmodes for each magnetic field line, as described by Rankin *et al.* [2006]. It has been shown by Kabin *et al.* [2007] and Kabin *et al.* [2008] that the polarizations of the natural field line vibrations in this case are no

longer aligned with a coordinate plane (such as the poloidal and toroidal directions in the case of a dipole field). Rather, the polarizations vary with position along a field line, and from field line to field line. This variation has been shown to be consistent with in-situ measurements of an FLR made by the THEMIS satellites [Sarris *et al.*, 2009]. In the special case where $\nabla\alpha$ is perpendicular to $\nabla\beta$, (for example, in a pure dipole magnetic field), then \mathbf{G} becomes diagonal, and the wave equation (11) reduce to those of Rankin *et al.* [2000] and Allan and Knox [1979a].

[12] The generalization of equations (11) and (13) to the general cold plasma case where field-aligned currents are included in the background magnetic field model is an area of ongoing research. A model which solves for the shear Alfvén and slow magnetosonic wavefield aligned eigenfunctions for a warm plasma MHD equilibrium (in which field aligned currents are allowed) is presented by Cheng and Zaharia [2003]. The continuum of eigenfrequencies calculated in that paper (for the cold plasma case) is shown to resemble the Alfvén speed profile, and no features attributed to field aligned currents are discussed. The specific effects of field aligned currents on the power coupling to FLRs and FLR characteristics remains an open question.

2.2. Magnetic Field Model, Coordinate System, and Alfvén Speed

[13] A simple analytical model for a compressed dipole field that has the desired properties of no field aligned current and day/night asymmetry is the vacuum magnetic field model of Stern [1985]. In this model, a dipole field representing Earth's magnetic field is contained within a conducting paraboloid shell that represents the magnetopause. Surface currents (representing Chapman-Ferraro currents) flowing along this shell cancel the component of the Earth's magnetic field normal to the surface, preventing magnetic flux from crossing the boundary. As the field within the magnetosphere in this model is curl-free, we set σ equal to unity in equation (8), which provides a further simplification to the wave equations (11) and (13). We follow the method of Stern [1985] to determine an analytic expression for γ and calculate the magnetic field, as described in detail in Appendix A.

[14] Having obtained \mathbf{B} and γ , we use numerical field line tracing to obtain the Euler potential coordinates α and β , initializing each field line on a dipole coordinate grid defined at the northern ionosphere, where $\alpha = \sin^2\theta/r_i$ and $\beta = \phi$. Here θ and ϕ are spherical coordinate colatitude and azimuthal angles, respectively, and r_i is the geocentric radius to the top of the ionosphere. Figures 1a and 1b show the coordinate grid derived from the magnetic field model in the noon-midnight meridian and equatorial planes, respectively. Note that lines of constant γ and α are perpendicular, illustrating the fact that the metric coefficient $g^{\alpha\gamma} = 0$ in Figure 1a. However, lines of constant β are swept antisunward as the outer boundary is approached in Figure 1b; hence $g^{\alpha\beta} \neq 0$. The metric coefficients g^{ij} are obtained numerically, by first forming the Jacobian matrix $\partial(x, y, z)/\partial(\alpha, \beta, \gamma)$ by finite differencing the cartesian coordinate locations of the (α, β, γ) grid, then inverting the result to obtain $\partial(\alpha, \beta, \gamma)/\partial(x, y, z)$. The rows of this matrix give the vectors $\nabla\alpha$, $\nabla\beta$, and $\nabla\gamma$, from which g^{ij} are calculated.

[15] Lastly, the plasma mass density $\rho(\alpha, \beta, \gamma)$ must be specified in order to calculate the Alfvén speed $v_A = B/\sqrt{\mu_0\rho}$. For the purposes of this paper, we consider the cold magnetospheric plasma density profile to be given by

$$\rho = \rho_{eq}(R)(r/R)^{-p}, \quad (14)$$

where r is the geocentric radius of a point on a field line (i.e., parameterized by constant α and β) that crosses the equatorial plane ($\gamma = 0$) at $r = R$, and the parameter p is the plasma mass index [Menk et al., 1999]. The equatorial mass density profile is assumed to follow a power law in R :

$$\rho_{eq}(R) = \rho_0(R/R_0)^{-q}, \quad (15)$$

where $\rho_{eq} = \rho_0$ at $R = R_0$ and q is a profile scaling parameter. A simple model for a plasmopause density step between R_1 and R_2 is given by setting $\rho_{eq} = \rho_1^{(1-w)}\rho_2^w$, where ρ_1 and ρ_2 are given by equation (15), using different values for ρ_0 and q at $R = R_1$ and R_2 . Here w is a function of R that equals unity for $R \leq R_1$, equals zero for $R \geq R_2$ and varies smoothly from 0 to 1 in between to represent the transition in parameters across the plasmopause.

2.3. Solving the Wave Equations

[16] We seek to solve equations (11) and (13) in response to a constant frequency driver located at the outer boundary, for the magnetic field configuration and Alfvén speed profile described in the previous section. Following the approach taken by Degeling and Rankin [2008] for a purely dipolar field, we assume that wave solutions can be expressed as a sum over a set of basis functions (f_n and h_n , n integer) local to each field line, multiplied by equatorial amplitudes (X_n and Y_n),

$$E_\alpha = \sum_{n=1}^N X_n(\alpha, \beta, t) f_n(\alpha, \beta, \gamma) e^{-i\omega t} \quad (16)$$

$$E_\beta = \sum_{n=1}^N Y_n(\alpha, \beta, t) h_n(\alpha, \beta, \gamma) e^{-i\omega t}, \quad (17)$$

where ω is the driver frequency. The amplitudes X_n and Y_n are assumed to vary slowly with time, such that $|\dot{X}_n| \ll \omega^2 |X_n|$ (and similarly for Y_n), in which case X_n and Y_n describe the amplitude of the wave envelope in E_α and E_β within which oscillations at the frequency ω occur. The basis functions used in this model respectively satisfy:

$$\left(g^{\alpha\alpha} f_n'\right)' + \frac{\omega_{fn}^2 \sqrt{g}}{v_A^2} g^{\alpha\alpha} f_n = 0; \quad \int_{\gamma_S}^{\gamma_N} \frac{\sqrt{g}}{v_A^2} g^{\alpha\alpha} f_n f_k d\gamma = \delta_{nk} \quad (18)$$

$$\left(g^{\beta\beta} h_n'\right)' + \frac{\omega_{hn}^2 \sqrt{g}}{v_A^2} g^{\beta\beta} h_n = 0; \quad \int_{\gamma_S}^{\gamma_N} \frac{\sqrt{g}}{v_A^2} g^{\beta\beta} h_n h_k d\gamma = \delta_{nk}, \quad (19)$$

where ω_{fn} and ω_{hn} are eigenfrequencies, and γ_N (γ_S) are boundary values for γ corresponding to the northern (southern) ionosphere. We use infinite Pederson conductance boundary conditions to calculate the f_n and h_n , which enforce nodes at the ionospheres, and result in purely real-

valued functions and eigenvalues. We note that, as long as the ionospheric conductance at either end of a field line is higher than the critical conductance ($\Sigma_{pc} = 1/\mu_0 v_{Ai}$, where v_{Ai} is the Alfvén speed at the ionosphere), the eigenfunction boundary values remain reasonably approximated by nodes, however finite conductance also introduces dissipation, which provides an ionospheric sink to ULF wave power. We wish to include this latter effect while keeping the simplicity of nodal boundary values for f_n and h_n . To this end we add a phenomenological imaginary part to the driver frequency $\omega = \omega_R + i\nu$, where:

$$\frac{2\nu}{\omega} = 1 - \left(\frac{\Sigma_p - \Sigma_{pc}}{\Sigma_p + \Sigma_{pc}}\right)^2. \quad (20)$$

This expression is obtained by considering the ionospheric reflection coefficient for the wave electric field, which is given by the term in brackets in the above expression [Scholer, 1970]. The functions f_n and h_n are calculated once the magnetic field and Alfvén velocity are defined, and are considered time-invariant in this problem.

[17] We now turn to calculating the time-dependent amplitudes of the basis functions. The general procedure, which is based on the spectral method, is outlined in the following, and a more complete description is given in Appendix B. In order to obtain a set of equations that can be solved numerically, we substitute equations (16) and (17) for the electric field into the top row of equation (11) (using equation (13) for \dot{b}_γ on the right-hand side), then multiply by each of the functions f_k in turn ($k = 1$ to N), and integrate the result over γ from the northern to southern ionosphere. In so doing, a series of N coupled PDEs for X_n and Y_n as a function of α , β and t is formed. Another set of N coupled equations is provided in a similar fashion by multiplying the bottom row of equation (11) by h_k ($k = 1$ to N) and integrating.

[18] The next step is to Fourier transform over the β coordinate, such that X_n and Y_n are expanded into a discrete series of Fourier components:

$$X_n = \sum_{m=-M}^M \langle X_n \rangle_m e^{im\beta}, \quad (21)$$

where

$$\langle X_n \rangle_m = \frac{1}{2\pi} \int_0^{2\pi} X_n e^{-im\beta} d\beta, \quad (22)$$

and similarly for Y_n . This results in a set of $2N \times (2M + 1)$ coupled PDEs for $\langle X_n \rangle_m$ and $\langle Y_n \rangle_m$ as a function of α and t only. These sets of equations can be compactly written as matrix equations (equations (B7) and (B8) in Appendix B), which are solved using an implicit finite differencing scheme.

[19] The inner and outer boundary conditions are formulated using the WKB approximation for the wave modes. At the inner boundary (maximum α) evanescent solutions are expected, and the WKB theory provides an estimation of the skin depth. At the outer boundary, the wave amplitudes are expressed in terms of an inward propagating wave source, with a wave number spectrum given by

WKB. The amplitude spectrum of the wave source is specified according to:

$$E_{\alpha s} = X_s(\beta, t)f_1(\alpha_o, \beta, \gamma)e^{-i\omega t}; \quad E_{\beta s} = Y_s(\beta, t)h_1(\alpha_o, \beta, \gamma)e^{-i\omega t}, \quad (23)$$

where ω is the driver frequency, and X_s and Y_s are the amplitudes of the fundamental eigenmodes along the outer boundary (at $\alpha = \alpha_o$), and the amplitude of higher spatial harmonics are set to zero. Following the approach of *Degeling et al.* [2008], the amplitude Y_s is given a functional form to represent the salient features of the wave source. For example, a localized peak in the distribution of wave power (that might result from magnetopause buffeting due to a wave packet of coherent structures in the solar wind) with phase fronts propagating away from the peak can be represented as follows:

$$Y_s(\beta, t) = Y_{so}(\beta)e^{i\varphi(\beta)}\left(1 - e^{-t/\tau_1}\right)e^{-t/\tau_2}, \quad (24)$$

where τ_1 and τ_2 specify the risetime and decay of the wave packet, $Y_{so}(\beta) = Y_{\max}\exp(-(\beta - \beta_o)^2/\Delta\beta^2)$ and $\varphi(\beta) = m_o((\beta - \beta_o) + \Delta\beta^2)^{1/2}$. Here $\Delta\beta$ defines the spatial width of a gaussian profile source centered at β_o , and m_o defines the rate of phase propagation far from the source. In order to model a propagating wave source along the magnetopause morning or afternoon flank (e.g., that might arise from over-reflection, or Kelvin-Helmholtz instability), $Y_{so}(\beta) = Y_{\max}|\beta|\exp(-(\beta - \beta_o)^2/\Delta\beta^2)$ and $\varphi(\beta) = \pm m_o(\beta - \beta_o)$ are used. Here the $|\beta|$ term is to ensure that the source has zero amplitude at noon and is symmetric about this point. The Fourier transform of this function gives $\langle Y_s \rangle$, and the WKB approximation of the wave equation is used to give $\langle X_s \rangle$ in terms of $\langle Y_s \rangle$. In all cases it is important that the Fourier spectrum of the source lies within the range of m values used to describe the wavefields (i.e., $\pm M$).

[20] In this model we take advantage of north/south symmetry in the magnetic field, plasma density profile and ionospheric boundary conditions, therefore $\gamma_S = -\gamma_N$ in equations (18) and (19), and it can be shown that all the basis functions for which n is odd (i.e., those with antinodes in the equatorial plane), are decoupled from those for which n is even (which have nodes in the equatorial plane). Given that the ULF wave source used in this model has an anti-node at the equatorial plane, only the odd numbered basis functions have nonzero amplitudes. Therefore all the even numbered modes are removed from the model, and the index n is understood to refer to the odd modes only. The results generated in this paper are produced with $n = 1, 3$ and 5 , and m values ranging from -8 to $+8$, giving a total of 102 undetermined basis functions amplitudes to be calculated as a function of α and t .

3. Results

3.1. Dependence of FLR Amplitude on ULF Source Location

[21] In this section, we examine the effect of scanning the azimuthal position of a constant frequency source at the magnetopause boundary on the relative amplitude of FLRs excited within the magnetosphere. The dayside magneto-

pause location and shape for this study are specified by the sub-solar and dawn/dusk stand-off distances (x_{mp} and y_{mp} , respectively, cf. Appendix A), which are given the values $x_{mp} = 10R_E$ and $y_{mp} = 15R_E$. This sets the configuration of the magnetic field and numerical grid used in the model, which is illustrated in Figure 1. The plasma mass density profile is specified by $p = 0$ in equation (14) and $q = 3$, $\rho_o = 750$ amu/cc and $R_o = 3R_E$ in equation (15).

[22] The ULF waves in this study are excited by a constant amplitude driver with a frequency of 5 mHz. The ULF wave source is given a gaussian profile in β , with width $\pi/4$, and the center β_o was scanned from 0 to $3\pi/4$ (i.e., 12–21 h MLT). Equatorial maps for the amplitude and phase of E_α and E_β are shown in Figure 2. These maps show that sharp amplitude peaks in E_α form and are accompanied by a phase change of π radians across the peak, as expected for field line resonance structures with low azimuthal mode number (“toroidal mode”).

[23] Figure 2 shows that the amplitude of FLR peaks is not a uniform function of MLT, and moreover, varies with the azimuthal location of the source. Figure 2 shows that the $n = 1$ peak is strongest for source locations near noon and becomes weaker as the source is moved along the dusk flank. The opposite trend appears to be the case for the higher harmonics $n = 3$ and $n = 5$. The equatorial maps of $|E_\beta|$ in Figure 2, in which the radiation pattern is dominated by the MHD fast wave, indicate that in each case the relative strength of the FLRs depends on the accessibility of MHD fast wave power to the resonant location. For example, fast waves launched close to local noon form a standing wave between the earth and noon magnetopause, allowing the excitation of the fundamental mode at low L shell. However, as the source is moved along the dusk flank, the fast waves propagate down-tail and refract away from the Earth at higher L shell, as indicated by the maps of E_β phase in Figure 2. For this reason, a ULF wave source localized along the flank more strongly couples to the harmonics than the fundamental mode FLR.

[24] Figure 2 has important implications for the possibility of electron energization by ULF waves: that the penetration of ULF wave power to low L shells from a source located along the magnetopause requires the source to be positioned close to local noon. This may preclude the Kelvin-Helmholtz instability during high solar wind streams as a significant source of power for electron transport to L shells below geosynchronous orbit, since the sites of excitation in this case are usually in the afternoon or morning sectors [*Rae et al.*, 2005; *Mann et al.*, 2002].

[25] Overlaid on the plots in Figure 2 are the resonant surfaces for the odd-numbered eigenmodes given by equations (18) and (19) ($\omega = \omega_{fn}$ and $\omega = \omega_{hn}$), and also the resonant surfaces for corresponding generalized SAW eigenfunctions of *Rankin et al.* [2006] (i.e., modes with antinodes in the equatorial plane). Figure 2 shows very close agreement between the amplitude peak in E_α and curves for $\omega = \omega_{fn}$. The resonance surfaces for the generalized SAW eigenfunctions also agree closely with the $\omega = \omega_{fn}$ and $\omega = \omega_{hn}$ curves, such that the SAW resonant surfaces are completely hidden in the plot. It is expected that these sets of curves should match along the noon and midnight meridians (assuming planar symmetry about this meridian), because $g^{\alpha\beta} = 0$ in this case and the eigen-

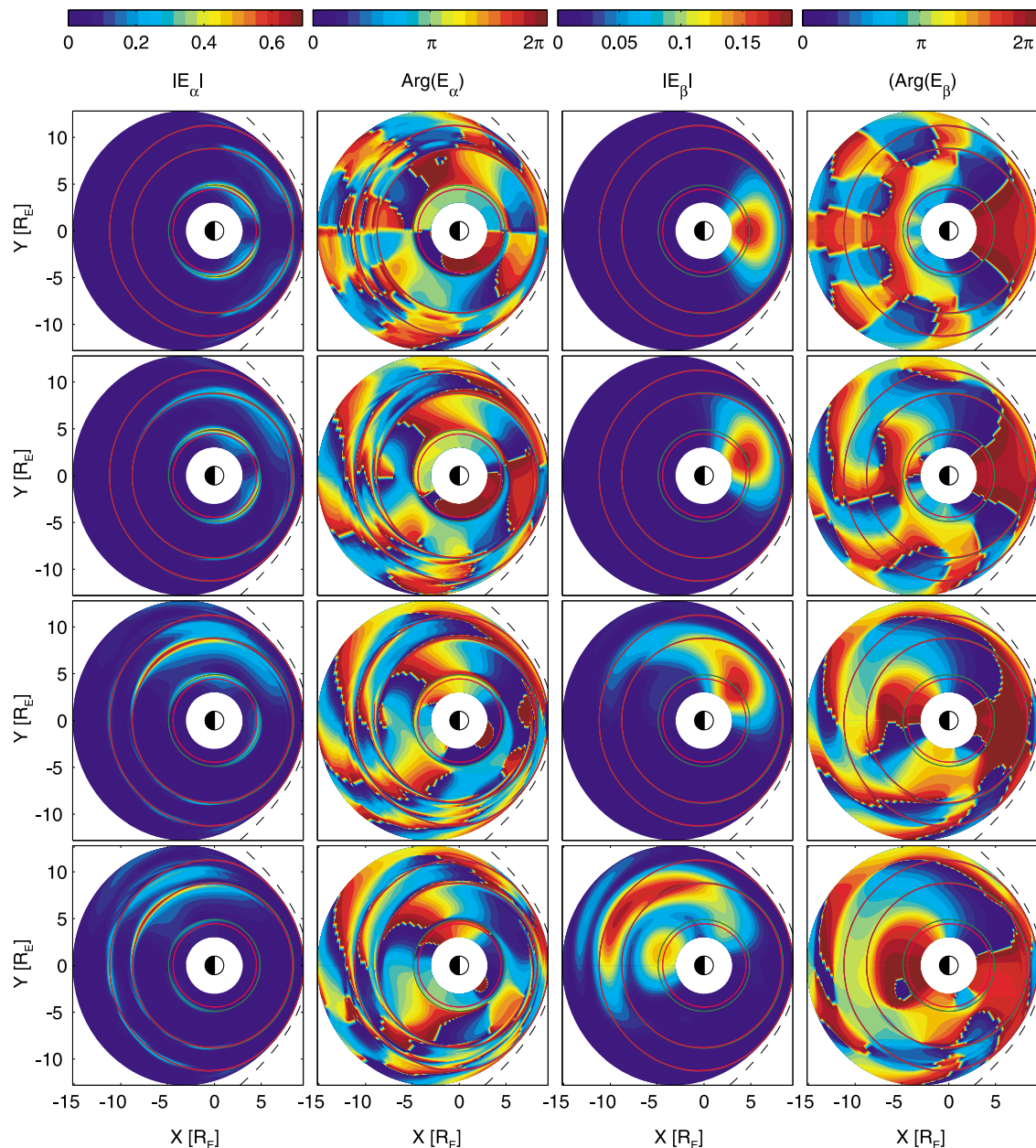


Figure 2. Equatorial maps of the amplitude and phase of E_α and E_β , respectively (from left to right), for a ULF wave source placed at 12, 15, 18, and 21 h MLT (from top to bottom, respectively). Red and green curves: resonant surfaces for the basic functions h_n and f_n , respectively. Note: these curves overlap for $n = 3$ and 5. The resonant surfaces for the corresponding SAW eigenmodes [cf. Rankin *et al.*, 2006] are completely overlaid by the respective curves for h_n and f_n .

function equations become formally equivalent. However the apparent agreement off this symmetry plane requires some explanation: At these locations, $\omega = \omega_{fn}$ and $\omega = \omega_{hn}$ curves lie between the pair of corresponding SAW resonance surfaces. In the case of the higher harmonics shown in Figure 2, these pairs of SAW resonant surfaces are very closely spaced and are indistinguishable in the figure. The curves for $\omega = \omega_{fn}$ and $\omega = \omega_{hn}$ are squeezed between these pairs, hence the close agreement. For the fundamental modes occurring at lower L shell in the figure, the pair of SAW resonant surface are well separated, and in this case

agree closely with their corresponding $\omega = \omega_{fn}$ and $\omega = \omega_{hn}$ curves because $g^{\alpha\beta}$ is sufficiently small that the eigenfunction solutions are qualitatively similar.

[26] The results of Figure 2 raise the question of the coupling efficiency of different azimuthal modes to field line resonances, which has been investigated previously for axis-symmetric models [Allan *et al.*, 1986; Zhu and Kivelson, 1988]. In each of the cases shown, the same amplitude spectrum is used to prescribe the ULF wave source, and different relative phases move the peak of the source to different MLTs. The change in FLR amplitude with source location demon-

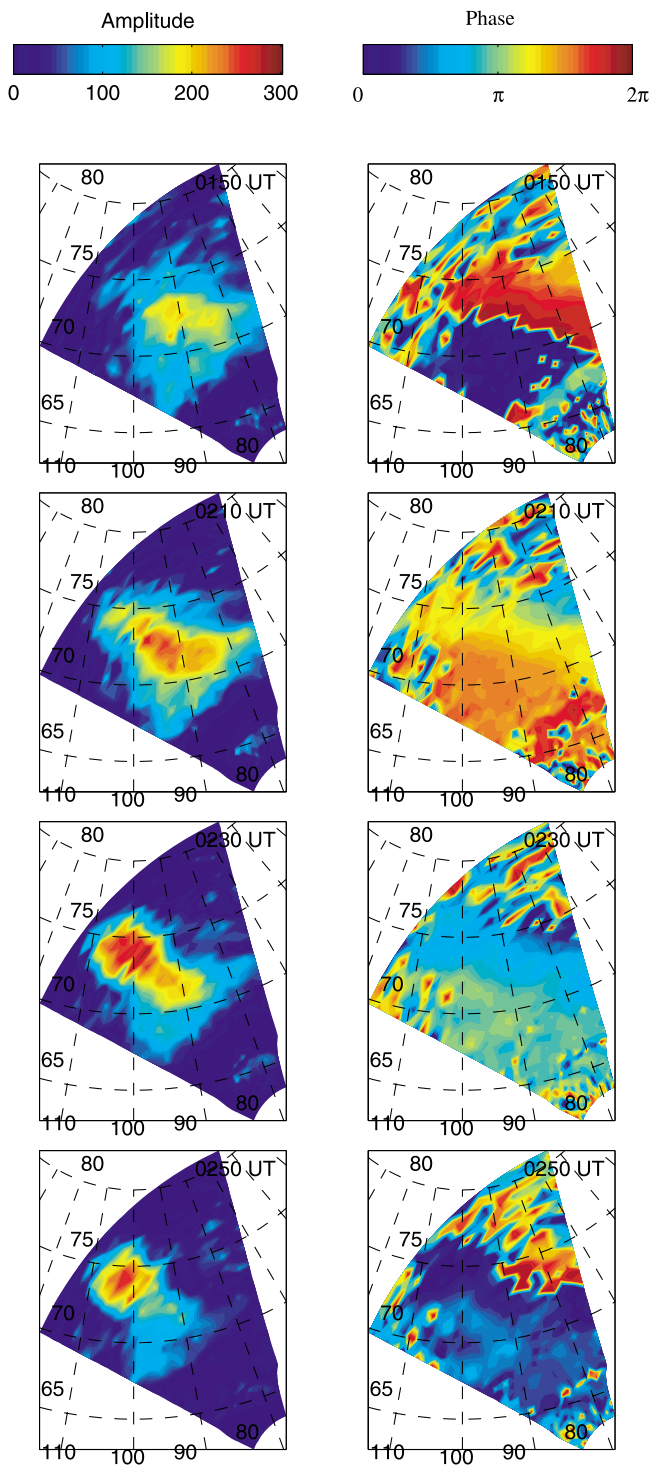


Figure 3. (left) Amplitude and (right) phase of Prince George SuperDARN ionospheric line of sight velocity measurements, between 0150 and 0250 UT on 25 November 2001. Each beam/range gate time series has been filtered with a band pass between 1.3 and 1.6 mHz to produce these maps.

strates that the notion of FLR coupling efficiency as a function of azimuthal mode number is complicated by the coupling between azimuthal modes when axis-symmetry is lost. This issue is a subject of continuing research.

3.2. Comparison With Observations on 25 November 2001

[27] A long interval of narrow band ULF wave activity was observed by a number of ground and space-based instruments during the recovery phase of a large geomagnetic storm, on 24 and 25 November 2001, and has been described by *Rae et al.* [2005, 2007b]. During the interval from 0100 to 0400 UT on 25 November, a favorable alignment of Polar, Cluster and geosynchronous satellites, in conjunction with the CANOPUS magnetometer chain and several SuperDARN radar observations, combine to provide convincing evidence that a large amplitude FLR at 1.5 mHz in the dusk sector was excited via fast MHD waves generated by the Kelvin-Helmholtz instability and/or overreflection along the afternoon flank of the magnetopause [e.g., *Mann et al.*, 1999].

[28] Figure 3 shows a series of line-of-sight (l-o-s) ionospheric (E and F region) plasma velocity measurements taken by the Prince George SuperDARN radar, between 0130 and 0300 UT on 25 November 2001. The time series data were filtered using a 1.3–1.6 mHz bandpass filter to produce the figures. Each plot in the left (right) column shows a map of the l-o-s velocity amplitude (phase) over the area covered by the radar, in Altitude Adjusted Corrected Geomagnetic Coordinates (AACGM) coordinates. The four images shown are separated in time by half an hour, and show the appearance of a large amplitude peak (close to $MLAT = 70^\circ$, $MLONG = -70^\circ$) with a 180° degree phase change across the peak, indicating an FLR structure. As time during the interval progresses, and Prince George station traverses the late afternoon sector (approximately 1600–1730 MLT), this structure elongates and migrates to exit to the left of the image ($MLAT = 75^\circ$, $MLONG = -100^\circ$). A secondary signature of a 1.5 mHz ULF wave is observed at low latitude ($MLAT \approx 65^\circ$) in the E region ionosphere. This signal exhibits a sharp phase change across some evidence of an amplitude peak, which may possibly represent another FLR of the same frequency at a lower L shell.

[29] As this is precisely the scenario addressed by our model, we use the observations during this interval to constrain the input parameters for the wave model, in an attempt to reconstruct the spatial characteristics of the ULF wave source and produce a global view of the distribution of ULF wave power during this event. In order to specify the day-side magnetopause location and shape during the interval of interest, mean solar wind velocity, magnetic field strength and dynamic pressure values were taken from ACE and WIND satellite observations (cf. Figure 3 of *Rae et al.* [2005]) and input to the empirical magnetopause model of *Shue et al.* [1997]. The resulting magnetopause shape was found to correspond approximately with the paraboloid defined by $x_{mp} = 10R_E$ and $y_{mp} = 15R_E$ (hence these values remain unchanged from the previous study).

[30] The ULF wave frequency was set to 1.5 mHz in accordance with the spectral peak occurring in the time series of a number of ground and space-based observations of the FLR during the interval of interest, (cf. Figure 10 of *Rae et al.* [2005]). The plasma mass density was adjusted to alter the position of the fundamental mode and higher har-

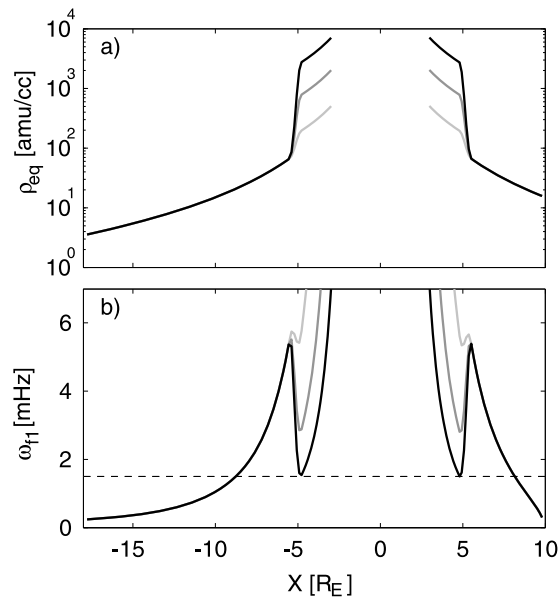


Figure 4. (a) Plasma mass density profiles along the noon/midnight meridian, in which the plasmaspheric density is increased to produce an increasingly sharp transition at the plasmopause. (b) The corresponding Alfvén continuum for toroidal modes. The dashed line indicates the driver frequency. Resonances occur at intersections between the solid and dashed lines.

monic resonant surfaces for this frequency. This was done by projecting the resonant surfaces, indicated by the locus of points where $\omega = \omega_{fn}$, along field lines onto the ionosphere, and adjusting the parameters in equation (15) to obtain an approximate fit with the amplitude peaks occurring in the SuperDARN Prince George observation in the afternoon sector.

[31] It is interesting to investigate whether the ULF wave model may be able to help in the interpretation of the lower latitude amplitude peak occurring in the Prince George observations; is it possible for this peak to be a second FLR, or is it more likely that this is an artefact of the E region radar signal? A natural first guess was to adjust the density profile to fit the $n = 1$ resonance to the weaker peak at lower latitude, and the $n = 3$ resonance to the stronger, higher latitude peak. However the equatorial density value required to achieve this at the higher latitude peak (approximately 300 amu/cc) is unreasonably high for an L shell mapping to that latitude. Moreover, assuming a power law density profile constrained by the two resonance positions, the $n = 5$ resonant surface lies well within the field of view of the Prince George radar, which is clearly absent from the observation.

[32] An alternative hypothesis that appears to fit the available observations is offered by including a sharp density drop associated with a well defined plasmopause in the model. In this case the plasmopause location is set to correspond approximately with the low-latitude peak and the $n = 1$ resonance location is constrained by the high-latitude peak. Figure 4 shows example density profiles constrained in this way, in which the plasmopause density gradient is increased. The corresponding fundamental mode Alfvén

continuum shown in Figure 4b illustrates that if the density gradient at the plasmopause is sufficiently large (black solid line in the plot), the continuum eigenfrequency profile for the $n = 1$ mode approaches the 1.5 mHz driver frequency close to the plasmopause location, producing an additional $n = 1$ resonance location. It should also be noted that, for the density profiles shown (in which $\rho \propto R^{-2.5}$ outside the plasmopause) the $n = 3$ and $n = 5$ resonances lie outside the dayside magnetosphere.

[33] The ULF wave model was run using the plasma density configuration described above (using the black solid curve in Figure 4a), for a number of cases in which the magnetopause source location and width were varied. Based on the interpretation made by *Rae et al.* [2005], we used the source amplitude and phase variation ($Y_{so}(\beta)$ and $\varphi(\beta)$ in equation (24)) to mimic waves arising from the Kelvin Helmholtz instability. A reasonable reproduction of the amplitude distribution of the high-latitude peak in the Prince George data was found using a ULF wave source with a peak amplitude at 1500 MLT, a width of ± 3 h, and phase variation across the source corresponding to $m_o = 2$. The temporal variation of the source was set using $\tau_1 = 2\pi/\omega$ and $\tau_2 = 10\pi/\omega$ in equation (24). Figure 5 shows a sequence of frames taken at half-hour intervals of the equatorial amplitude and phase of E_α projected along-field lines onto the ionosphere, for field lines within the field of view of the Prince George SuperDARN radar. These frames show the development, elongation and subsequent decay of the high-latitude FLR structure within the field of view of the radar, in qualitative agreement with the observations. A second, much weaker peak and corresponding change in phase occurs at lower latitude, indicating another FLR. The position of this FLR corresponds with the plasmopause location, as expected for the tailored density profile. The relative amplitudes of the high- and low-latitude resonances in the model qualitatively agrees with the SuperDARN observations. A broad peak also appears and decays at higher latitude within the radar field of view, which is not present in the observations. This peak does not have a corresponding phase change and is therefore not associated with an FLR, but rather the constructive interference of MHD fast waves. It was found that the relative size of this peak compared to the FLR could be reduced by decreasing the ionospheric wave damping rate (by raising Σ_p in equation (20)), however this also increased the sharpness of the FLR peaks, making them significantly more narrow in latitude than the observed peaks in the Prince George data. It is expected that these discrepancies (the narrow FLR structure and also the broad peak at higher latitude) could be mitigated by a more realistic treatment of the ionospheric boundary condition.

[34] Figure 6 shows equatorial maps of E_α amplitude and phase at 0200 UT, and shows that the high-latitude FLR extends from the early afternoon (peak at $L = 7.9$) well into the late evening sector, (peak at $L = 9.1$). This is consistent with ground-based magnetometer observations of a large-amplitude FLR in the evening sector by the CANOPUS magnetometer chain (located +2.5 h MLT from the Prince George radar) and also Polar satellite electric and magnetic field observations (situated close to the equatorial plane, $L \approx 9$, 19h MLT during the interval of interest) reported by *Rae et al.* [2005]. Using the Tsyganenko 89 magnetic

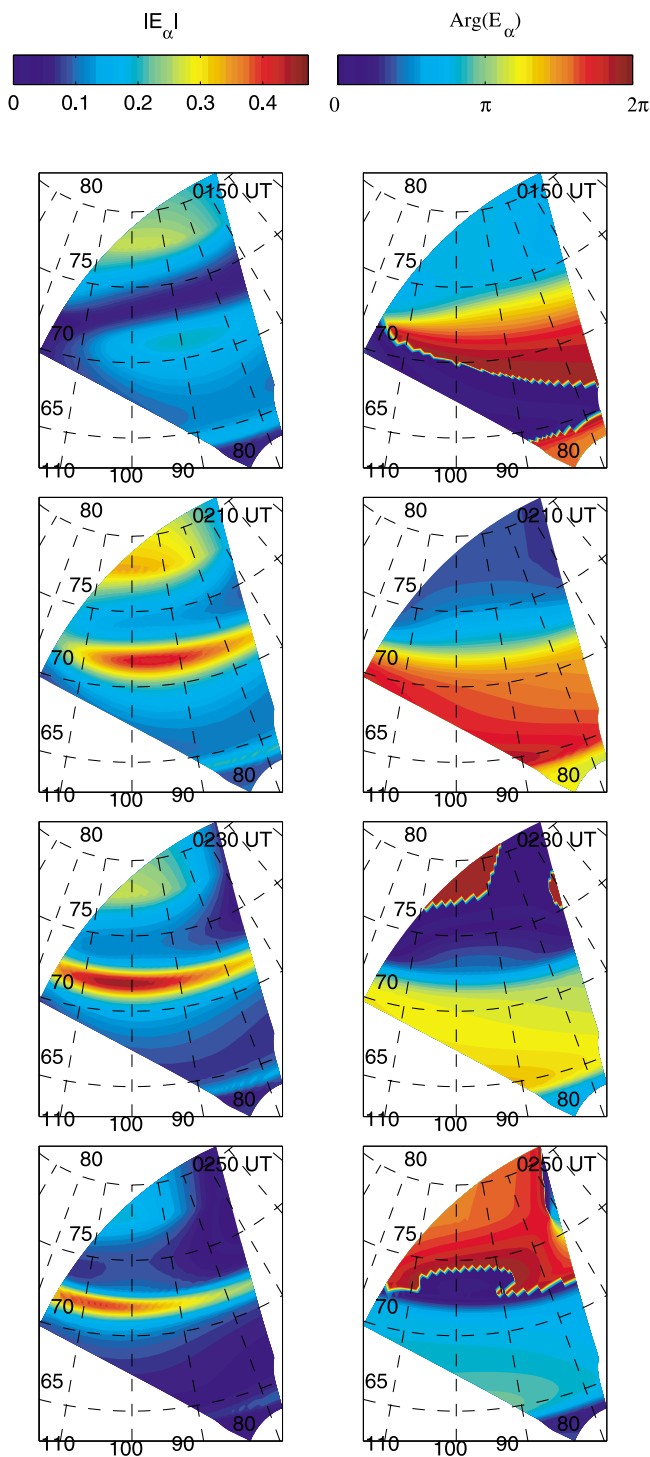


Figure 5. Maps of the (left) amplitude and (right) phase of E_α produced by the model and projected to the ionosphere along field lines corresponding to the field of view of the Prince George radar for times corresponding to those shown in Figure 3.

field model, these authors find that the mapping of the Polar observation to the ionosphere corresponds closely with the FLR peak measured on the ground by the CANOPUS magnetometers. It should be noted that, while

the magnetospheric location of the FLR in the current model is in agreement with the inferred location from Polar, a similar field line mapping to the ionosphere at high L shell in the dusk to midnight sector using the magnetic field model described in this paper would be invalid, because of the absence of magnetic field stretching from cross-tail currents. However, in principle the ULF wave model equations described in this paper can be applied to magnetic fields that include a cross-tail current, as long as $\mathbf{B} \cdot \mathbf{J} = 0$. This extension of the wave model is the subject of ongoing research.

3.3. Polarization Properties of Driven FLRs

[35] The scenario of 25 November 2001 provides a good opportunity to investigate the polarization properties of FLRs predicted by this ULF wave model, and compare against the polarizations of the generalized eigenfunctions of Rankin *et al.* [2006]. This particular case is interesting because the fundamental modes of Rankin *et al.* [2006] for these conditions are characterized by strong changes in polarization as a function of MLT (similar to those at high L shell reported by Kabin *et al.* [2007]). To this end, the ULF wave model was run until the MHD fast mode had decayed to 10% of its peak value, and the electric field vector was interpolated along the peak in E_α corresponding to the high-

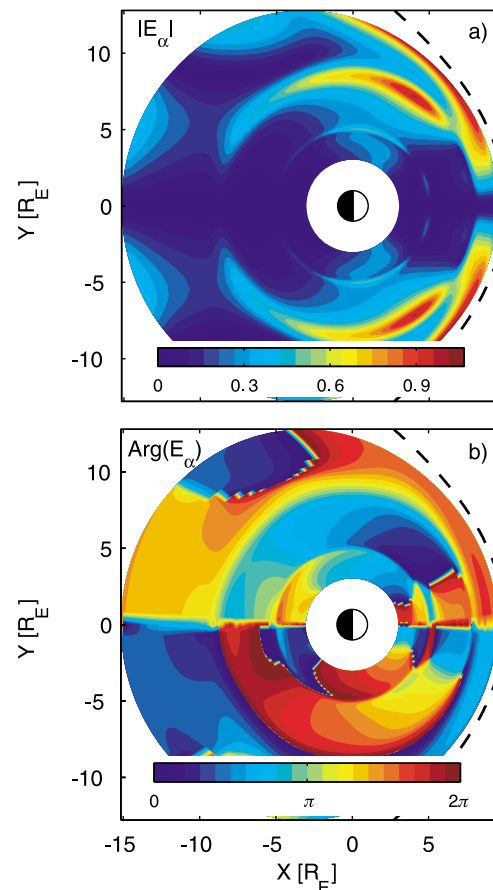


Figure 6. Equatorial maps of (a) E_α amplitude (arb. units) and (b) phase (radians) for the 25 November model run, at 0200 UT.

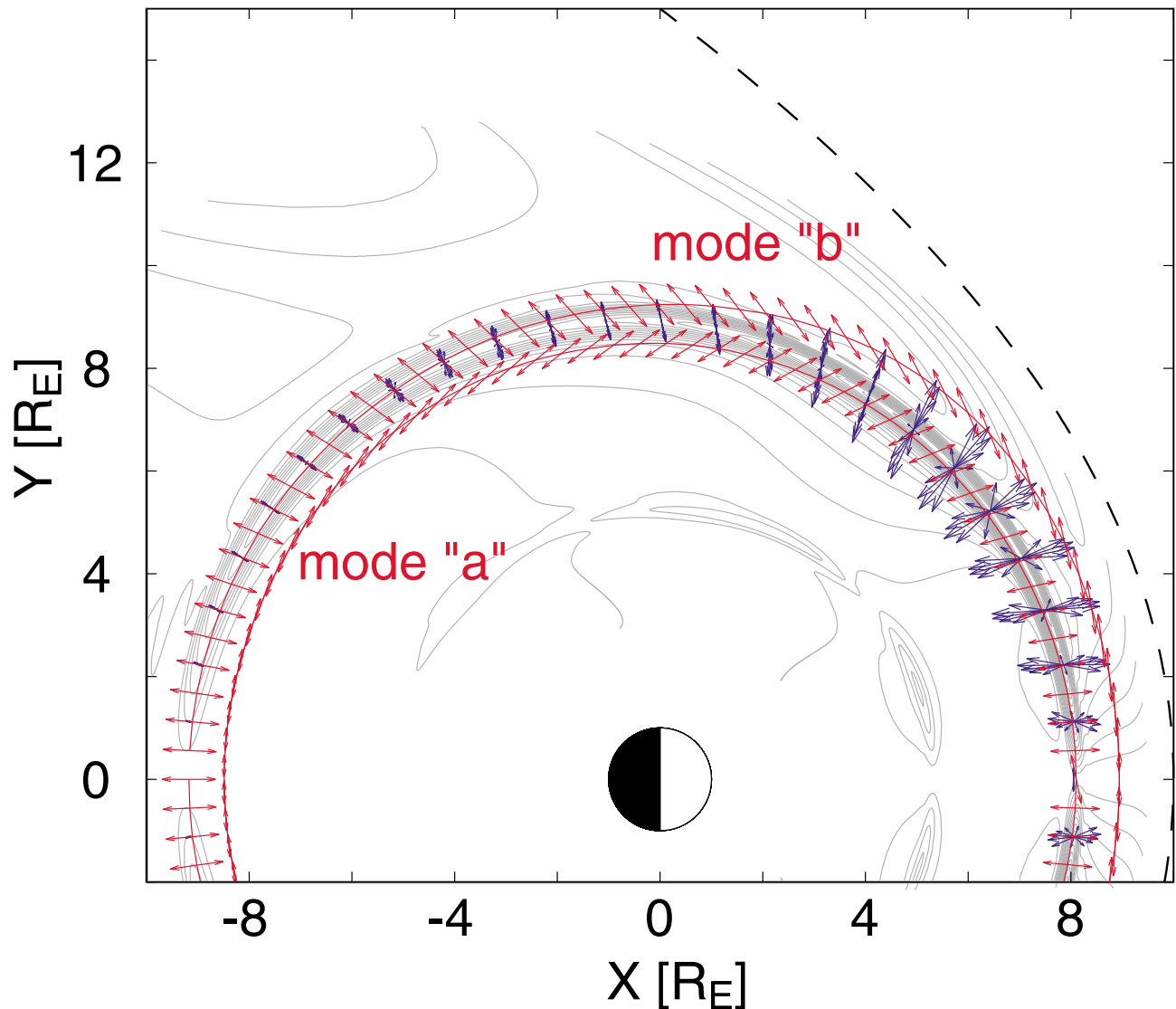


Figure 7. Gray contours: equatorial amplitude of E_α showing the FLR, taken 3 h after the start of the run, by which time the driver had dropped to 10% of its peak value; blue vectors: equatorial electric field along the FLR peak, at various phases; red vectors: equatorial polarization of the generalized SAW eigenfunctions (modes “a” and “b”) along their resonance surfaces (solid red lines); dashed line: the magnetopause boundary.

latitude FLR. Figure 7 shows the vector electric field for different phases during the final period of the simulation. Also shown are contours of $|E_\alpha|$ showing the FLR peak, and the resonant surfaces and equatorial polarizations for the generalized SAW eigenfunctions of Rankin *et al.* [2006] (here labeled mode “a” and mode “b”). This figure shows that the peak in $|E_\alpha|$ corresponds closely with the resonant surface for mode “a” close to local noon, however as MLT is increased the peak moves between the resonant surfaces, and converges with mode “b” as local midnight is approached. The polarization of the electric field along the FLR peak is elliptical over most of the afternoon sector,

where the remnant of the MHD fast mode is still significant, and tends toward linear polarization in the postdusk sector. The direction of the polarization vector along the FLR peak varies with MLT, however it does not vary as strongly as either of the two modes “a” or “b.” Rather, the direction remains approximately poloidal (radial) and appears to converge with the polarization of mode “a” in the early afternoon, and mode “b” in the late evening, as the FLR peak converges with the respective resonant surfaces in each case. This appears to suggest an answer to the question posed in section 4 of Kabin *et al.* [2007] regarding the polarization properties of FLRs resonantly excited by MHD

fast modes: namely that low m fast modes (considered in this paper) appear to couple most strongly to the mode which has its polarization closest to the poloidal direction on any given field line (i.e., mode “a” near local noon, and mode “b” in local midnight in this example), and do not appear to exclusively excite a specific generalized SAW eigenfunction.

4. Conclusion

[36] In this paper, we have introduced a new model for ULF waves in a compressed dipole magnetosphere, in which cold plasma MHD fast waves driven by a narrow-band wave source along the magnetopause couple power to FLRs within the magnetosphere. The wave equations on which the model is based are shown to be valid for magnetic fields in which field-aligned currents (associated with the background field) are zero. As an example, we use the vacuum magnetic field model of *Stern* [1985] in this paper.

[37] The ULF wave model is used to investigate how the efficiency of resonantly coupling power to either the fundamental mode FLR or its spatial harmonics depends on the location of the ULF wave power source along the magnetopause. The model results demonstrate that the spatial characteristics of FLRs are determined by the accessibility of MHD fast waves from the magnetopause source to locations within the inhomogeneous magnetosphere. We therefore use the wave model to infer the spatial characteristics of a ULF wave source during an interval of ULF activity on 25 November 2001, by constraining the source parameters and plasma density profile based on SuperDARN radar observations during the interval. We find that an anti-sunward propagating ULF wave source peaked in the mid-afternoon sector of the magnetopause most closely reproduces the salient features of the observations, suggesting that the source driving mechanisms may be Kelvin-Helmholtz instability.

[38] These results are clearly dependent on magnetic field and plasma density inhomogeneities specific to the scenarios considered. This demonstrates the need to account for these inhomogeneities when assessing the effects of ULF waves, for example, on radiation belt electron transport.

Appendix A: Magnetic Field Model Equations

[39] The studies used in this paper are based on a magnetic field model in which a dipole field representing Earth’s magnetic field is contained within a conducting paraboloid shell that represents the magnetopause. Surface currents (known as Chapman-Ferraro currents) flowing along this shell cancel the component of the Earth’s magnetic field normal to the surface, preventing magnetic flux from crossing the boundary. As there are no interior current sources, the curl of the magnetic field within the magnetosphere is zero, and the field may be represented by the gradient of a scalar potential $\gamma = \gamma_E + \gamma_{mp}$ where γ_E is the contribution from a dipole field representing the Earth, and γ_{mp} is the contribution from magnetopause currents. The scalar potential must satisfy Laplace’s equation in order to give a divergence-free magnetic field. Following the method of *Stern* [1985], we use orthogonal parabolic coordinates to

calculate γ_{mp} , which are given in terms of solar magnetospheric (SM) cartesian coordinates (x, y, z) by:

$$\begin{aligned} \lambda^2 &= r + (x - x_o) \\ \mu^2 &= r - (x - x_o) \\ \tan\psi &= z/y \\ r^2 &= (x - x_o)^2 + y^2 + z^2 \end{aligned} \quad (A1)$$

where the origin of the coordinate system is located at $x = x_o, y = z = 0$. The magnetopause boundary is given by $\lambda = \lambda_o$ (a constant). The parameters x_o and λ_o specify the location and shape of the magnetopause boundary. For example, the subsolar standoff distance is given by $x_{mp} = 1/2(\lambda_o^2 + 2x_o)$, and the radial distance to the magnetopause from any point along the dawn/dusk meridian is given by $y_{mp} = \lambda_o(\lambda_o^2 + 2x_o)^{1/2}$.

[40] Laplace’s equation is separable in parabolic coordinates, and allows a general solution to be expressed in terms of a sum over trigonometric and Bessel functions. For the purposes of this paper, we consider the dipole tilt to be zero with respect to the x - z plane, in which case *Stern* [1985] shows that γ_{mp} is given by:

$$\gamma_{mp} = \sin\psi \sum_n a_n J_1(k_n \mu) I_1(k_n \lambda), \quad (A2)$$

where J_1 and I_1 are Bessel and modified Bessel functions, respectively, and k_n satisfies $J_1(k_n A) = 0$, where A is a parameter that controls the spatial range over which the expansion is valid. The values of the coefficients a_n are determined by applying the boundary condition that $\partial\gamma_{mp}/\partial\lambda|_{\lambda=\lambda_o} = -\partial\gamma_E/\partial\lambda|_{\lambda=\lambda_o}$ in order to zero the magnetic field component perpendicular to the surface where $\lambda = \lambda_o$.

[41] The magnetic field is given by $\mathbf{B} = \mathbf{B}_{mp} + \mathbf{B}_E$, where \mathbf{B}_E is the dipole field of the Earth and \mathbf{B}_{mp} is given by:

$$\mathbf{B}_{mp} = -\nabla\gamma_{mp} = -\frac{\partial\gamma_{mp}}{\partial\lambda}\nabla\lambda - \frac{\partial\gamma_{mp}}{\partial\mu}\nabla\mu - \frac{\partial\gamma_{mp}}{\partial\psi}\nabla\psi, \quad (A3)$$

where $\nabla\lambda, \nabla\mu$ and $\nabla\psi$ are obtained from equation (A1).

Appendix B: Solving the Wave Equation Using the Spectral Method

[42] With the solutions E_α and E_β decomposed into a series of basis functions f_n and h_n , the problem is now reduced to finding the time-dependent amplitudes X_n and Y_n , assuming the slowly varying approximation described in section 2.3. Before proceeding, we emphasize that the functions defined by equations (18) and (19), which have polarizations aligned with the coordinate basis vectors $\nabla\alpha$ and $\nabla\beta$ are not equivalent to the SAW eigenfunctions of *Rankin et al.* [2006], which are given by setting the right hand side (RHS) of equation (11) to zero. The choice of basis in this paper is made for numerical reasons.

[43] Substituting equations (16) and (17) into the top row of equation (11), multiplying the result by f_k , where k is

scanned from 1 to N , and integrating over γ results in a series of N equations, which can be combined into a single matrix equation:

$$\Omega_f \cdot X + (\Psi - \Phi) \cdot Y + \frac{2i}{\omega} (\dot{X} + \Psi \cdot \dot{Y}) = \frac{e^{i\omega t}}{\omega^2} \int_{\gamma_S}^{\gamma_N} f \cdot \frac{\partial \dot{b}_\gamma}{\partial \beta} d\gamma, \quad (\text{B1})$$

where $X = [X_1 \dots X_n]^T$ is a column vector of length N and similar definitions are used for Y, f and h . The matrices Ω_f, Ψ and Φ are defined by:

$$\Omega_f = \left(I - \frac{\omega_f^2}{\omega^2} \right) \cdot \left(\int_{\gamma_S}^{\gamma_N} \frac{\sqrt{g}}{v_A^2} g^{\alpha\beta} f \cdot f^T d\gamma \right) = \left(I - \frac{\omega_f^2}{\omega^2} \right) \quad (\text{B2})$$

$$\Psi = \int_{\gamma_S}^{\gamma_N} \frac{\sqrt{g}}{v_A^2} g^{\alpha\beta} f \cdot h^T d\gamma \quad (\text{B3})$$

$$\Phi = \int_{\gamma_S}^{\gamma_N} f \cdot \left(g^{\alpha\beta} h'^T \right)' d\gamma = - \int_{\gamma_S}^{\gamma_N} g^{\alpha\beta} f' \cdot h'^T d\gamma, \quad (\text{B4})$$

where ω_f is a diagonal $N \times N$ matrix formed from ω_{f_m} , and similarly for ω_h . The last result above comes from using integration by parts and noting that $g^{\alpha\beta} = 0$ at $\gamma = \gamma_N$ and $\gamma = \gamma_S$. Similarly it can be shown, starting with the bottom row of equation (11), multiplying by h and integrating over γ , that:

$$(\Psi^T - \Phi^T) \cdot X + \Omega_h \cdot Y + \frac{2i}{\omega} (\Psi^T \cdot \dot{X} + \dot{Y}) = - \frac{e^{i\omega t}}{\omega^2} \int_{\gamma_S}^{\gamma_N} h \cdot \frac{\partial \dot{b}_\gamma}{\partial \alpha} d\gamma, \quad (\text{B5})$$

where

$$\Omega_h = \left(I - \frac{\omega_h^2}{\omega^2} \right) \cdot \left(\int_{\gamma_S}^{\gamma_N} \frac{\sqrt{g}}{v_A^2} g^{\beta\beta} h \cdot h^T d\gamma \right) = \left(I - \frac{\omega_h^2}{\omega^2} \right). \quad (\text{B6})$$

At this point we have two sets of N coupled PDEs in α, β and t . By taking advantage of the cyclic coordinate β we can expand the solution using a discrete spectrum of $2M + 1$ azimuthal modes (i.e., mode numbers from $-M$ to $+M$). This results in a set of $N \times (2M + 1)$ PDEs, which are functions of α and t only. This can be expressed in block-matrix form, where the matrices have $(2M + 1) \times (2M + 1)$ blocks, with each block having $N \times N$ elements. In the following we will use angular brackets $\langle \rangle$ to indicate

the Fourier transform over β , e.g., $X = \sum_{m=-M}^M \langle X \rangle_m e^{im\beta}$, where $\langle X \rangle_m = 1/2\pi \int_0^{2\pi} X e^{-im\beta} d\beta$. Hence $\langle X \rangle_m$ as the m^{th}

segment of a column vector of length $N \times (2M + 1)$ elements: $\langle X \rangle = [\langle X \rangle_{-M} \dots \langle X \rangle_M]$. The $(m, k)^{\text{th}}$ block of the Fourier transform of an $N \times N$ matrix (e.g., Ω_f) is defined by: $\langle \Omega_f \rangle_{mk} = 1/2\pi \int_0^{2\pi} \Omega_f e^{-i(m-k)\beta} d\beta$.

[44] Multiplying equations (B1) and (B5), respectively, by $e^{-i\beta/2\pi}$, using equation (13) for the RHS in each case, and integrating over β can then be shown to give:

$$\sum_{k=-M}^M \left(\langle \Omega_f \rangle_{lk} - \zeta_{lk} \right) \cdot \langle X \rangle_k + \langle \lambda \rangle_{lk} \cdot \langle Y \rangle_k - \eta_{lk} \cdot \frac{\partial}{\partial \alpha} \langle Y \rangle_k + \frac{2i}{\omega} \left(\langle \dot{X} \rangle_l + \langle \Psi \rangle_{lk} \cdot \langle \dot{Y} \rangle_k \right) = 0 \quad (\text{B7})$$

$$\sum_{k=-M}^M \langle \lambda^T \rangle_{lk} \cdot \langle X \rangle_k + \langle \Omega_h \rangle_{lk} \cdot \langle Y \rangle_k - \eta_{lk}^T \cdot \frac{\partial}{\partial \alpha} \langle X \rangle_k + \xi_{lk} \cdot \frac{\partial^2}{\partial \alpha^2} \langle Y \rangle_k + \frac{2i}{\omega} \left(\langle \Psi^T \rangle_{lk} \cdot \langle \dot{X} \rangle_k + \langle \dot{Y} \rangle_l \right) = 0, \quad (\text{B8})$$

where $l = -M \dots +M$, $\lambda = \Psi - \Phi$, and

$$\eta_{lk} = \sum_{m=-M}^M \frac{im}{\omega^2} \int_{\gamma_S}^{\gamma_N} \langle f \rangle_{l-m} \cdot \langle h^T \rangle_{m-k} d\gamma \quad (\text{B9})$$

$$\zeta_{lk} = \sum_{m=-M}^M \frac{m^2}{\omega^2} \int_{\gamma_S}^{\gamma_N} \langle f \rangle_{l-m} \cdot \langle f^T \rangle_{m-k} d\gamma \quad (\text{B10})$$

$$\xi_{lk} = \sum_{m=-M}^M \frac{1}{\omega^2} \int_{\gamma_S}^{\gamma_N} \langle h \rangle_{l-m} \cdot \langle h^T \rangle_{m-k} d\gamma. \quad (\text{B11})$$

In deriving the above expressions, the assumptions $\langle h^T \cdot (\partial Y / \partial \alpha) \rangle_m \gg \langle (\partial h^T / \partial \alpha) \cdot Y \rangle_m$, and $\langle f^T \cdot (\partial X / \partial \alpha) \rangle_m \gg \langle (\partial f^T / \partial \alpha) \cdot X \rangle_m$ have been used. That is, we assume variations in the α direction of the electric field components are primarily the result of changes in the amplitude of modes into which the components are decomposed (i.e., X and Y), rather than the structure of the modes themselves.

[45] The above two equations express the time evolution of a total of $(2M + 1) \times N$ modes for $\langle X \rangle$ and $\langle Y \rangle$ as a function of α . The inner and outer α boundary conditions for the above equations are as follows. At the boundary closest to the Earth (maximum α), evanescent solutions are expected, hence we assume each of the modes to satisfy $\partial / \partial \alpha (\langle Y \rangle) + \nu \cdot \langle Y \rangle = 0$. At the outer boundary (minimum α), we express the solution as a sum over incident and reflected waves, such that $\partial / \partial \alpha (\langle Y \rangle) + iK \cdot \langle Y \rangle = 2iK \cdot \langle Y_s \rangle$, where $\langle Y_s \rangle$ represent time dependent amplitudes for each incident wave mode, located at the outer boundary. The constants ν , and K are obtained by applying the WKB approximation to equations (B7) and (B8) at the inner and outer boundaries. This involves setting the time derivatives in these equations to zero, and differentiating equation (B7) with respect to α in order to eliminate $\langle X \rangle$ and $\partial / \partial \alpha \langle X \rangle$ in equation (B8). The resulting second-order linear differential equation for $\langle Y \rangle$ has solutions of the form $\exp(iK) \cdot \langle Y \rangle$ (where K is a square matrix) if the coefficients appearing in the equation are considered approximately constant. Carrying this procedure out, we find that K is diagonally dominant (and similarly for ν at the inner boundary), which allows us to simplify the boundary conditions in the model by removing the off-diagonal terms in these matrices.

[46] **Acknowledgments.** The authors would like to thank Richard Marchand and Ian Mann for many useful discussions during the development of the ULF wave model. This work is supported by the Canadian Space Agency Canadian Geospace Monitoring program and the Natural Sciences and Engineering Research Council of Canada.

[47] Robert Lysak thanks Jay Johnson and another reviewer for their assistance in evaluating this paper.

References

- Allan, W., and F. B. Knox (1979a), Dipole field model for axisymmetric Alfvén waves with finite ionosphere conductivities, *Planet. Space Sci.*, **27**(1), 79–85.
- Allan, W., and F. B. Knox (1979b), Effect of finite ionosphere conductivities on axisymmetric toroidal Alfvén wave resonances, *Planet. Space Sci.*, **27**(7), 939–950.
- Allan, W., and M. E. Poulter (1992), ULF waves—Their relationship to the structure of the Earth’s magnetosphere, *Rep. Progr. Phys.*, **55**, 533–598.
- Allan, W., S. P. White, and M. E. Poulter (1986), Hydromagnetic wave coupling in the magnetosphere-plasmapause effects on impulse excited resonances, *Planet. Space Sci.*, **34**, 1189–1200.
- Alperovich, L. S., and E. N. Fedorov (2007), *Hydromagnetic Waves in the Magnetosphere and the Ionosphere*, Springer, New York.
- Chen, L., and A. Hasegawa (1974), A theory of long-period magnetic pulsations: I. Steady state excitation of field line resonance, *J. Geophys. Res.*, **79**(7), 1024–1032, doi:10.1029/JA079i007p01024.
- Cheng, C., and S. Zaharia (2003), Field line resonances in quiet and disturbed time three-dimensional magnetospheres, *J. Geophys. Res.*, **108**(A1), 1001, doi:10.1029/2002JA009471.
- Degeling, A. W., and R. Rankin (2008), Resonant drift echoes in electron phase space density produced by dayside Pc5 waves following a geomagnetic storm, *J. Geophys. Res.*, **113**, A10220, doi:10.1029/2008JA013254.
- Degeling, A. W., L. G. Ozeke, R. Rankin, I. R. Mann, and K. Kabin (2008), Drift resonant generation of peaked relativistic electron distributions by Pc 5 ULF waves, *J. Geophys. Res.*, **113**, A02208, doi:10.1029/2007JA012411.
- D’haeseleer, W. D., W. N. G. Hitchon, J. D. Callen, and J. L. Shohet (1991), *Flux Coordinates and Magnetic Field Structure*, Springer, Berlin, Germany.
- Dobias, P., I. O. Voronkov, and J. C. Samson (2004), On nonlinear plasma instabilities during the substorm expansive phase onset, *Phys. Plasmas*, **11**, 2046–2053, doi:10.1063/1.1695357.
- Elkington, S. (2006), A review of ULF interactions with radiation belt electrons, in *Magnetospheric ULF Waves: Synthesis and New Directions*, *Geophys. Monogr. Ser.*, vol. 169, AGU, Washington, D. C.
- Kabin, K., R. Rankin, I. R. Mann, A. W. Degeling, and S. R. Elkington (2008), Polarization properties of the ULF waves in non-axisymmetric background magnetic fields, in *WSPC Proceedings*, *Adv. Geosci.*, vol. 14, World Sci., Singapore.
- Kabin, K., R. Rankin, I. R. Mann, A. W. Degeling, and R. Marchand (2007), Polarization properties of standing shear Alfvén waves in non-axisymmetric background magnetic fields, *Ann. Geophys.*, **25**, 815–822.
- Mann, I., et al. (2002), Coordinated ground-based and Cluster observations of large amplitude global magnetospheric oscillations during a fast solar wind speed interval, *Ann. Geophys.*, **20**(4), 405–426.
- Mann, I., A. Wright, K. Mills, and V. Nakariakov (1999), Excitation of magnetospheric waveguide modes by magnetosheath flows, *J. Geophys. Res.*, **104**(A1), 333–353, doi:10.1029/1998JA900026.
- Menk, F., D. Orr, M. Clilverd, A. Smith, C. Waters, D. Milling, and B. Fraser (1999), Monitoring spatial and temporal variations in the dayside plasmasphere using geomagnetic field line resonances, *J. Geophys. Res.*, **104**(A9), 19,955–19,969, doi:10.1029/1999JA900205.
- Rae, I. J., et al. (2005), Evolution and characteristics of global Pc5 ULF waves during a high solar wind speed interval, *J. Geophys. Res.*, **110**, A12211, doi:10.1029/2005JA011007.
- Rae, I. J., I. R. Mann, Z. C. Dent, D. K. Milling, E. F. Donovan, and E. Spanswick (2007a), Multiple field line resonances: Optical, magnetic and absorption signatures, *Planet. Space Sci.*, **55**, 701–713, doi:10.1016/j.pss.2006.02.009.
- Rae, I. J., C. E. J. Watt, F. R. Fenrich, I. R. Mann, L. G. Ozeke, and A. Kale (2007b), Energy deposition in the ionosphere through a global field line resonance, *Ann. Geophys.*, **25**, 2529–2539.
- Rankin, R., F. Fenrich, and V. T. Tikhonchuk (2000), Shear Alfvén waves on stretched magnetic field lines near midnight in Earth’s magnetosphere, *Geophys. Res. Lett.*, **27**(20), 3265–3268, doi:10.1029/2000GL000029.
- Rankin, R., K. Kabin, and R. Marchand (2006), Alfvénic field line resonances in arbitrary magnetic field topology, *Adv. Space Res.*, **38**, 1720–1729, doi:10.1016/j.asr.2005.09.034.
- Ray, E. C. (1963), On the Motion of Charged Particles in the Geomagnetic Field, *Ann. Phys.*, **24**(1), 1–18.
- Samson, J. C., J. A. Jacobs, and G. Rostoker (1971), Latitude-dependent characteristics of long-period geomagnetic micropulsations, *J. Geophys. Res.*, **76**(16), 3675–3683, doi:10.1029/JA076i016p03675.
- Samson, J. C., L. L. Cogger, and Q. Pao (1996), Observations of field line resonances, auroral arcs, and auroral vortex structures, *J. Geophys. Res.*, **101**(A8), 17,373–17,383, doi:10.1029/96JA01086.
- Sarris, T. E., et al. (2009), Characterization of ULF pulsations by THEMIS, *Geophys. Res. Lett.*, **36**, L04104, doi:10.1029/2008GL036732.
- Scholer, M. (1970), On the motion of artificial ion clouds in the magnetosphere, *Planet. Space Sci.*, **18**(7), 977–1004, doi:10.1016/0032-0633(70)90101-7.
- Shue, J.-H., J. K. Chao, H. C. Fu, C. T. Russell, P. Song, K. K. Khurana, and H. J. Singer (1997), A new functional form to study the solar wind control of the magnetopause size and shape, *J. Geophys. Res.*, **102**(A5), 9497–9511, doi:10.1029/97JA00196.
- Singer, H. J., D. J. Southwood, R. J. Walker, and M. G. Kivelson (1981), Alfvén-wave resonances in a realistic magnetospheric magnetic field geometry, *J. Geophys. Res.*, **86**(A6), 4589–4596, doi:10.1029/JA086iA06p04589.
- Southwood, D. J. (1974), Some features of field line resonances in the magnetosphere, *Planet. Space Sci.*, **22**, 483–491.
- Southwood, D. J., and W. J. Hughes (1983), Theory of hydromagnetic waves in the magnetosphere, *Space Sci. Rev.*, **35**, 301–366.
- Stern, D. P. (1976), Representation of magnetic fields in Space, *Rev. Geophys.*, **14**(2), 199–214.
- Stern, D. P. (1985), Parabolic harmonics in magnetospheric modeling—The main dipole and the ring current, *J. Geophys. Res.*, **90**(A11), 851–863, doi:10.1029/JA090iA11p10851.
- Walker, A. D. M. (1980), Modelling of Pc5 pulsation structure in the magnetosphere, *Planet. Space Sci.*, **28**, 213–223.
- Zhu, X. M., and M. G. Kivelson (1988), Analytic formulation and quantitative solutions of the coupled ULF wave problem, *J. Geophys. Res.*, **93**(A8), 8602–8612, doi:10.1029/JA093iA08p08602.

A. W. Degeling, F. R. Fenrich, K. Kabin, I. J. Rae, and R. Rankin, Department of Physics, University of Alberta, Edmonton, AB T6G 2G7, Canada. (degeling@phys.ualberta.ca)